ELECTROCHEMISTRY

Water-hydroxide trapping in cobalt tungstate for proton exchange membrane water electrolysis

Ranit Ram[1]†, Lu Xia[1]†, Hind Benzidi[2]†, Anku Guha[1]†, Viktoria Golovanova[1], Alba Garzón Manjón[3], David Llorens Rauret[3], Pol Sanz Berman[2], Marinos Dimitropoulos[1], Bernat Mundet[3], Ernest Pastor[4,5], Veronica Celorrio[6], Camilo A. Mesa[7], Aparna M. Das[1], Adrián Pinilla-Sánchez[1], Sixto Giménez[7], Jordi Arbiol[3,8], Núria López[2], F. Pelayo García de Arquer[1]*

The oxygen evolution reaction is the bottleneck to energy-efficient water-based electrolysis for the production of hydrogen and other solar fuels. In proton exchange membrane water electrolysis (PEMWE), precious metals have generally been necessary for the stable catalysis of this reaction. In this work, we report that delamination of cobalt tungstate enables high activity and durability through the stabilization of oxide and water-hydroxide networks of the lattice defects in acid. The resulting catalysts achieve lower overpotentials, a current density of 1.8 amperes per square centimeter at 2 volts, and stable operation up to 1 ampere per square centimeter in a PEMWE system at industrial conditions (80°C) at 1.77 volts; a threefold improvement in activity; and stable operation at 1 ampere per square centimeter over the course of 600 hours.

The increasing global energy demand, combined with the urgent need to abate climate change, has accelerated the development of sustainable and clean energy technologies as alternatives to fossil fuels. Water electrolysis (WE) to synthesize hydrogen (H_2) has emerged as a promising strategy to produce clean energy vectors from water and low-carbon electricity, offering a path to decarbonize global industries, such as energy, transport, manufacturing, and agriculture, among others (1–3).

Among the different WE technologies, the proton exchange membrane water electrolysis (PEMWE), in which cathode and anode electrodes are intimately connected through a proton conductive membrane, exhibits advantages compared with diaphragm- and anion transport–based alternatives in terms of productivity (high–current density operation), energy efficiency, stability, and levelized cost of H_2 (4–6). In this context, the efficient and sustainable large-scale production of H_2 through WE still faces important challenges. These are associated with the sluggish kinetics of the oxygen evolution reaction (OER) and the reliance on scarce, critical raw materials, such as iridium (Ir)—so far, the prevalent anode catalyst material because of its stability but one of the least-abundant metals on Earth (7–9).

Alternative approaches using ruthenium (Ru) have shown promising activity but suffer from a strong metal dissolution in acidic media intrinsic to lattice OER mechanisms (10–12). There is, thus, an urgent need to develop efficient and stable Ir- and Ru-free anodes for PEMWE (13–17).

Transition metal oxides are interesting catalyst candidates for the OER because their multiple oxidation states could promote activity in a wide pH range (18, 19). First-row transition metal oxides have shown promising activity in the acidic OER (20–25). Among them, Co-, Ni-, and Mn-based anodes have received special attention considering their relative abundance and activity prospects (26, 27). Based on theoretical calculations, the OER activity of Co-based oxides should be comparable to that of Ru- and Ir-based oxides (28).

However, such prospective activity is challenged by the limited stability of CoO_x in acid because of higher Co ion dissolution (Fig. 1A), even at open circuit potential (29, 30). Several strategies have been proposed to stabilize cobalt oxides in highly concentrated proton environments. Fundamental progress in this direction has mostly been pursued in low-current H cells controlling the valence and ratio of active species (e.g., Co^{2+}/Co^{3+}) through doping with higher-valence metals (e.g., Cr and Mn) (22, 24, 25, 31); controlling catalyst reconstruction (32); doping with hydrophobic carbon (33); and addressing the substrate-catalyst interaction (29).

Unfortunately, translating these findings into active and stable PEMWE based on more abundant alternatives to Ir and Ru remains an open challenge (34). In Mn systems, phase control (γ-MnO_2) led to stability improvements (12 hours at 100 mA cm^{-2}), which gradually decrease as the γ-MnO_2 phase becomes permanganate (MnO_4^-) (26). Mn-oxybromide species resulted in 300 hours of stability at 100 mA cm^{-2} (0.41–mV $hour^{-1}$ degradation) (23). In Co-based electrodes, La and Mn doping has enabled a ~0.6–A cm^{-2} current density at 2 V and 110 hours of stability at 210 mA cm^{-2} (~1.65 V at 80ºC) (25). These experimental observations showcase the challenges in achieving Ir- and Ru-free PEMWE anodes that break the activity-stability trade-off through conventional doping schemes.

Recent works have highlighted the potential of controlling the other half of the electrochemical interface (i.e., water structure and adsorbed oxide species) to improve the OER. The participation of oxygen from adsorbed water in the OER, as opposed to lattice-mediated, would decrease metal dissolution and increase stability (25). In general, the interaction of adsorbed bridging oxygen (O_{bri}) species with water could open previously unrealized reaction pathways (35). Theoretical studies have shown the critical role of the H bonding network of interfacial water and its impact on proton-electron transfer steps (36, 37). Decreasing the degree of H bonding of interfacial water (n–HB H_2O) has been predicted to reduce the activation energy needed to dissociate water (38). The role of interfacial water and the H bonding network, already studied for the hydrogen evolution reaction (39), is largely overlooked for acidic OER. This prompted us to jointly address the water and oxide structure, a so-far underexplored path, seeking to improve activity and stability in non-Ir PEMWE anodes.

In this work, we demonstrate control over the OER by modulating the interfacial water structure and intermediate species in a delaminated CoW oxide lattice (Fig. 1, B to D), resulting in active and stable PEMWE. We achieve this by implementing a delamination strategy whereby high-valence sacrificial elements, such as W, when incorporated in a $CoWO_4$ (CWO) crystal structure, could be selectively eliminated in a subsequent water-hydroxide-WO_4^{2-} anion exchange process (Fig. 1C). This results in structural delamination and the subsequent trapping and stabilization of water and hydroxide species in a Co oxide defect network. Such water-hydroxide shielding renders the Co ion dissolution thermodynamically unfavorable for the delaminated CWO in contrast to Co_3O_4 (Fig. 1D and table S1), which shows a marked decrease in Co ion dissolution in acid (fig. S1). The delaminated (CWO-del) catalysts achieve notable performance in a PEMWE, with a current density of 1.8 A cm^{-2} at 2 V—up to a threefold improvement compared with the previous best performance for non-Ir and/or non-Ru (25, 40)—and stable operation for 608 hours at the current density of 1 A cm^{-2} (Fig. 1, E and F).

[1]ICFO – Institut de Ciències Fotòniques, The Barcelona Institute of Science and Technology, 08860 Castelldefels, Barcelona, Spain. [2]ICIQ-CERCA – Institute of Chemical Research of Catalonia, The Barcelona Institute of Science and Technology, 43007 Tarragona, Spain. [3]Catalan Institute of Nanoscience and Nanotechnology (ICN2), CSIC and BIST, Campus UAB, Bellaterra, 08193 Barcelona, Catalonia, Spain. [4]CNRS, Université de Rennes, IPR (Institut de Physique de Rennes) - UMR 6251, Rennes, France. [5]CNRS, Université de Rennes, DYNACOM (Dynamical Control of Materials Laboratory) - IRL2015, The University of Tokyo, 7-3-1 Hongo, Tokyo 113-0033, Japan. [6]Diamond Light Source, Harwell Science and Innovation Campus, Didcot OX11 0DE, UK. [7]Institute of Advanced Materials (INAM), Universitat Jaume I, 12006 Castelló, Spain. [8]ICREA, Pg. Lluís Companys 23, 08010 Barcelona, Spain.

*Corresponding author. Email: pelayo.garciadearquer@icfo.eu
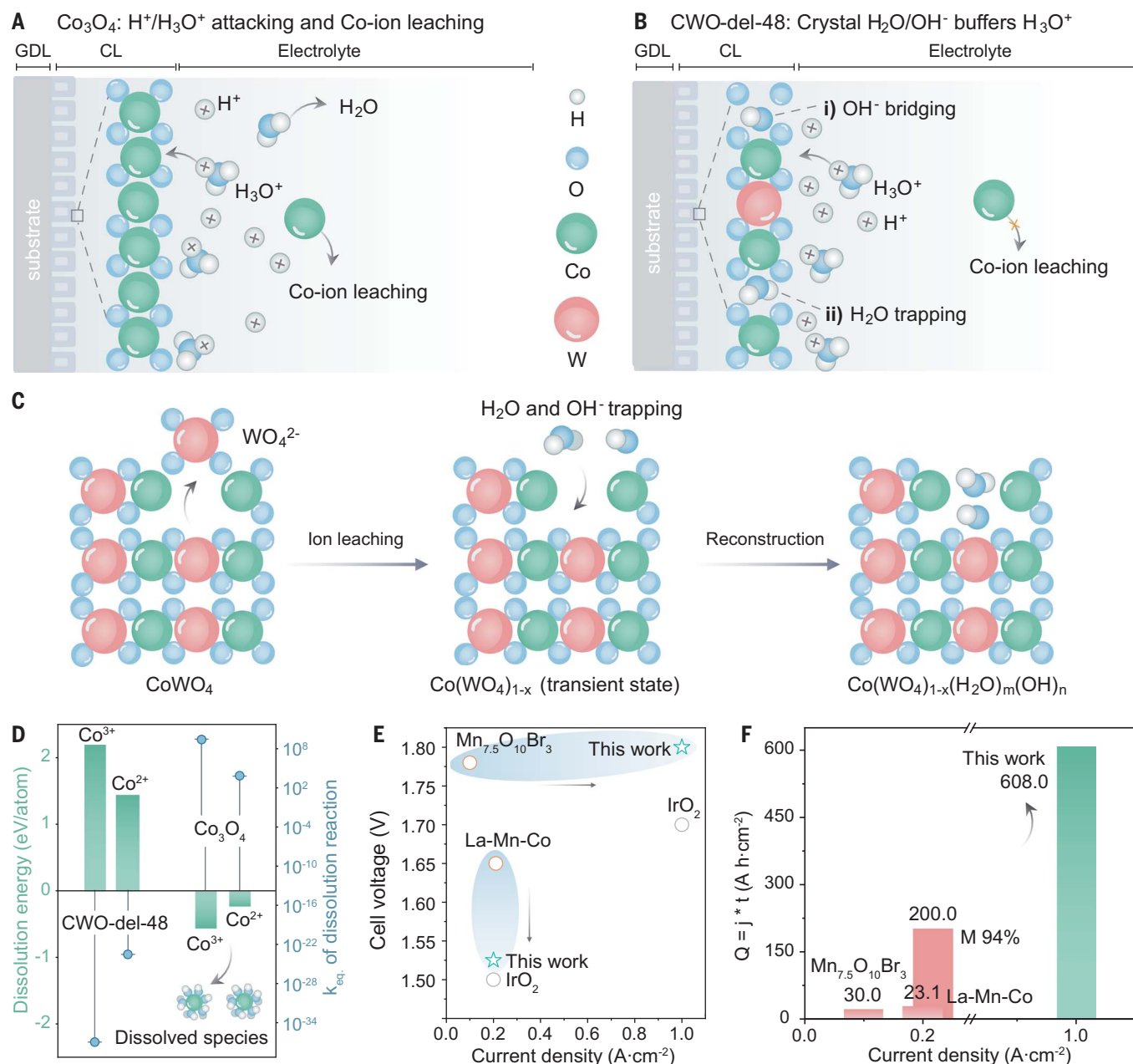†These authors contributed equally to this work.

Fig. 1. Water-hydroxide trapping enables active and stable PEMWE.
(**A**) Schematic illustration of the dissolution of Co ions in Co_3O_4 through Co–O bond cleaving, followed by their hydration in acidic medium. GDL, gas diffusion layer; CL, catalyst layer. (**B**) A depiction of delaminated cobalt catalysts (CWO-del-48), illustrating the effect of water trapping and hydroxide bridging within the crystal lattice, enabling stability in acid. (**C**) The process and crystallographic representation of CWO delamination into CWO-del-48 through base treatment. (**D**) CWO-del-48 catalyst shows unfavorable Co ion dissolution compared with Co_3O_4. The calculated equilibrium constants of the dissolution reaction for CWO-del-48, $k_{eq} \ll 1$, suggest nonspontaneity of the process. The structure of dissolved Co^{2+} and Co^{3+} ions are shown in the inset. (**E** and **F**) This equilibrium enables substantial advances in performance cell voltage versus current density (E) and durability (F) compared with state-of-the-art Ir- and Ru-free anodes in PEMWE.

Anion exchange delamination controls water structure in acid

To incorporate and stabilize OH^- and H_2O into the lattice of MM'_xO_y (where M is Mn, Co, Ni, or Cu), we devised an anion exchange strategy whereby lattice oxyanions (e.g., $M'_xO_y^{z-}$, where M' is S, Mo, or W) would be delaminated and exchanged by OH^- and H_2O species as follows

$$MM'_xO_y + mH_2O + nOH^- \rightarrow$$
$$M(M'_xO_y)_{1-q}(H_2O)_m(OH)_n + qM'_xO_y^{z-} \quad (1)$$
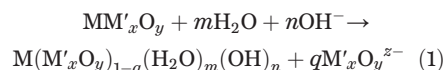
The design principles require that such oxyanions have adequate binding energies with OH^- and water species—conditions that promote their sacrificial leaching (41)—and that the host lattice could accommodate OH^- and H_2O

species to saturate the resulting oxyanion vacancies (supplementary text, section 4, and tables S4 to S6). Our initial theoretical calculations predicted that WO_4^{2-} ions, compared with other anions, such as molybdate or sulfate, provide more favorable defect energy to meet these criteria: The energy associated with defect formation upon removing WO_4^{2-} from the $CoWO_4$
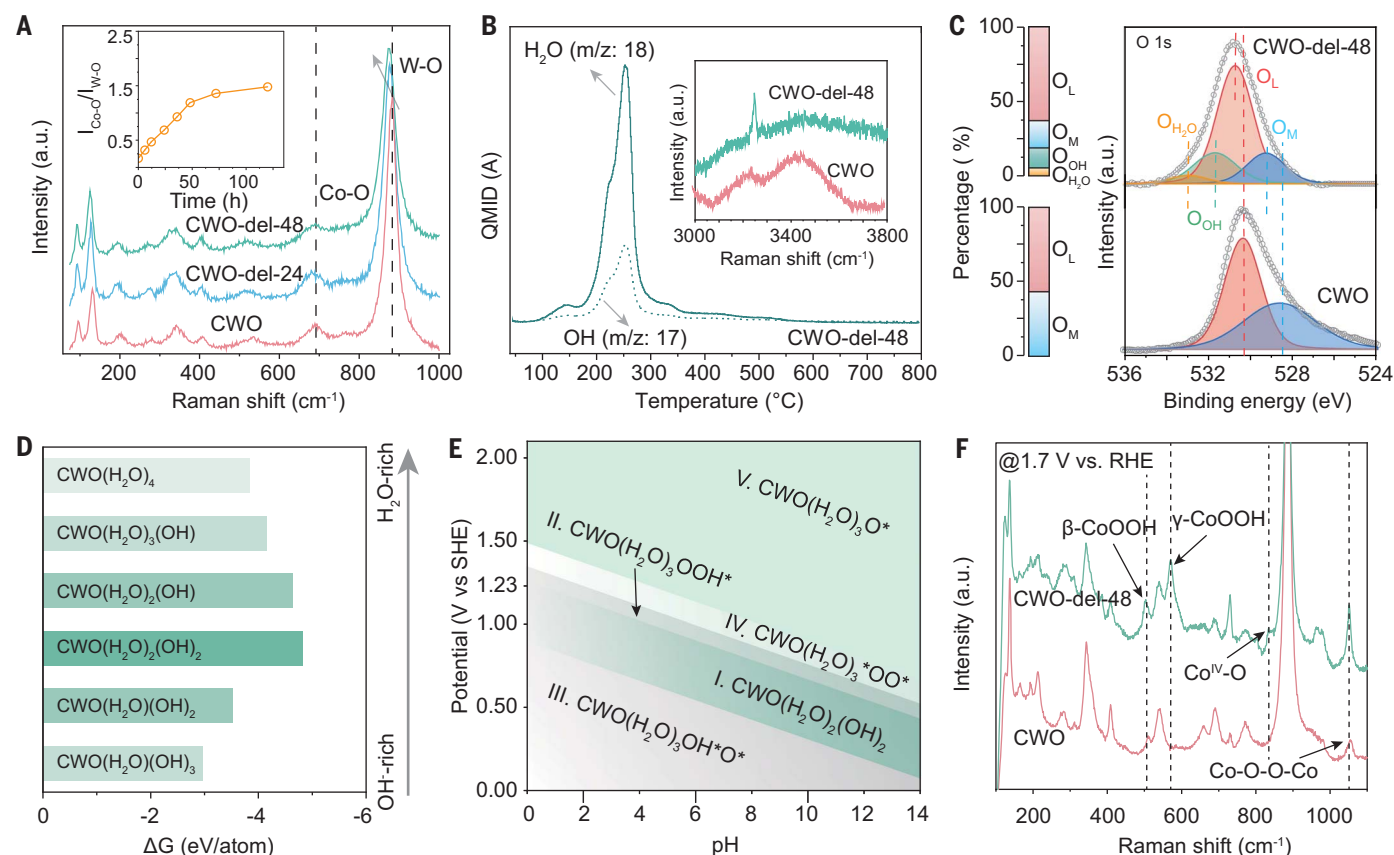
Fig. 2. Water trapping and hydroxide bridging. (**A**) Ex situ Raman spectra of as-synthesized CWO and CWO-del (24 hours and 48 hours) showing a regular red shift associated with the W−O vibrational peaks. (Inset) Intensity ratio of the Co−O and W−O peaks with delamination time. a.u., arbitrary units. (**B**) TGA-MS shows the presence of H_2O and hydroxide in CWO-del-48. (Inset) Ex situ Raman spectra showing presence of different types of water. The sharp H−OH stretching peak of CWO-del-48 indicates presence of strongly H-bonded water. QMID, quasi-multiple ion detection. (**C**) O 1s XPS spectra of CWO and CWO-del-48. O 1s peak in CWO deconvolutes into metal oxygen (O_M) and lattice oxygen (O_L). O 1s peak in CWO-del-48 deconvolutes into four peaks: O_M, O_L, hydroxide (O_{OH}), and water (O_{H2O}). (**D**) Visual representation of the free energy changes involved in the delamination process of CWO to $CWO(H_2O)_m(OH)_n$ under alkaline solution, as a result of water trapping and hydroxide bridging with the removal of tungstate (movie S1). DFT simulations predict that $CWO(H_2O)_2(OH)_2$ is thermodynamically the most favorable composition for CWO-del-48. (**E**) Potential and pH dependence of the intermediates in OER for the CWO-del-48. SHE, standard hydrogen electrode. (**F**) In situ Raman spectra of CWO and CWO-del-48 catalysts at 1.7 V versus RHE suggests the involvement of Co (III), Co (IV), and Co−peroxide as the active OER species.

is the lowest energy among SO_4^{2-} and MoO_4^{2-} removal from $CoSO_4$ and $CoMoO_4$, respectively (supplementary text, section 4, and fig. S2).

We thus synthesized CWO using a hydrothermal reaction (supplementary text, section 1, and fig. S3). The sharp peaks in x-ray diffraction (XRD) patterns from different batches indicate a highly crystalline structure matching a monoclinic $CoWO_4$ phase and the high reproducibility of the synthesis procedure (figs. S4 and S5).

To perform the $WO_4^{2-} \rightarrow OH^-$ and H_2O anion exchange, we explored a base treatment dispersing the resulting CWO material in an 0.1 M potassium hydroxide (KOH) aqueous solution for different time periods (supplementary text, section 3, and figs. S6 and S7). We studied the effects of cation (Li^+ to Cs^+), solvent [H_2O, dimethyl sulfoxide (DMSO), or N-methylpyrrolidone (NMP)], and pH (both experimental and the-

oretical) in the process (supplementary text, section 3, and figs. S8 to S13). This study revealed the critical role of K^+ to balance the delamination and the need for H_2O and hydroxide to enable the anion exchange. CWO-del samples retained structural stability after 72 hours of immersion in 0.5 M H_2SO_4 as opposed to Co controls (fig. S14).

Powder XRD patterns show a regular shift in the most intense $\bar{1}11$ peak (table S7), indicating the generation of defects or strain in the crystal structure, whereas the bulk monoclinic crystal phase remains intact. These are consistent with optoelectronic, magnetic, and x-ray absorption spectroscopy studies that show the increased formation of vacancies and defects (figs. S15 to S19).

Transmission electron microscopy (TEM) and scanning transmission electron microscopy (STEM) images show a shape transition

from a cube-like CWO (figs. S20 and S21) to a delaminated, flake-like shape after KOH treatment (figs. S22 and S23). The size of the particles after delamination remains comparable to CWO (fig. S24).

High-resolution TEM (HRTEM) images reveal the missing regular (010) crystal plane in CWO-del-48 (figs. S22 and S25), indicative of defects arising from WO_4^{2-} leaching. High–annular angle dark-field STEM (HAADF-STEM) images, and respective energy-dispersive x-ray spectroscopy (EDX) mapping of Co and W, show the uniform distribution of Co and W throughout the pristine and delaminated nanocrystals (figs. S26 and S27). The electron energy-loss spectroscopy (EELS) spectra indicate a reduction in the Co/W atomic ratio after delamination (fig. S28). Additionally, atomic force microscopy (AFM) reveals missing planes and corresponding defects in CWO-del-48 (figs.

S29 to S31), in agreement with HRTEM and STEM results.

To assess the atomic arrangement of Co and W sites, we performed integrated differential phase contrast (iDPC) STEM (fig. S32). CWO samples exhibit a regular atomic arrangement of Co, W, and O atoms, consistent with a monoclinic phase. CWO-del-48, on the other hand, reveals a substantial number of vacancies due to WO_4^{2-} leaching (fig. S33).

To get more insights into the dynamics of the oxyanion exchange, we performed ex situ Raman spectroscopy measurements at different delamination times. These reveal a bathochromic shift (~5 to 10 cm^{-1}) for both Co–O (~690 cm^{-1})
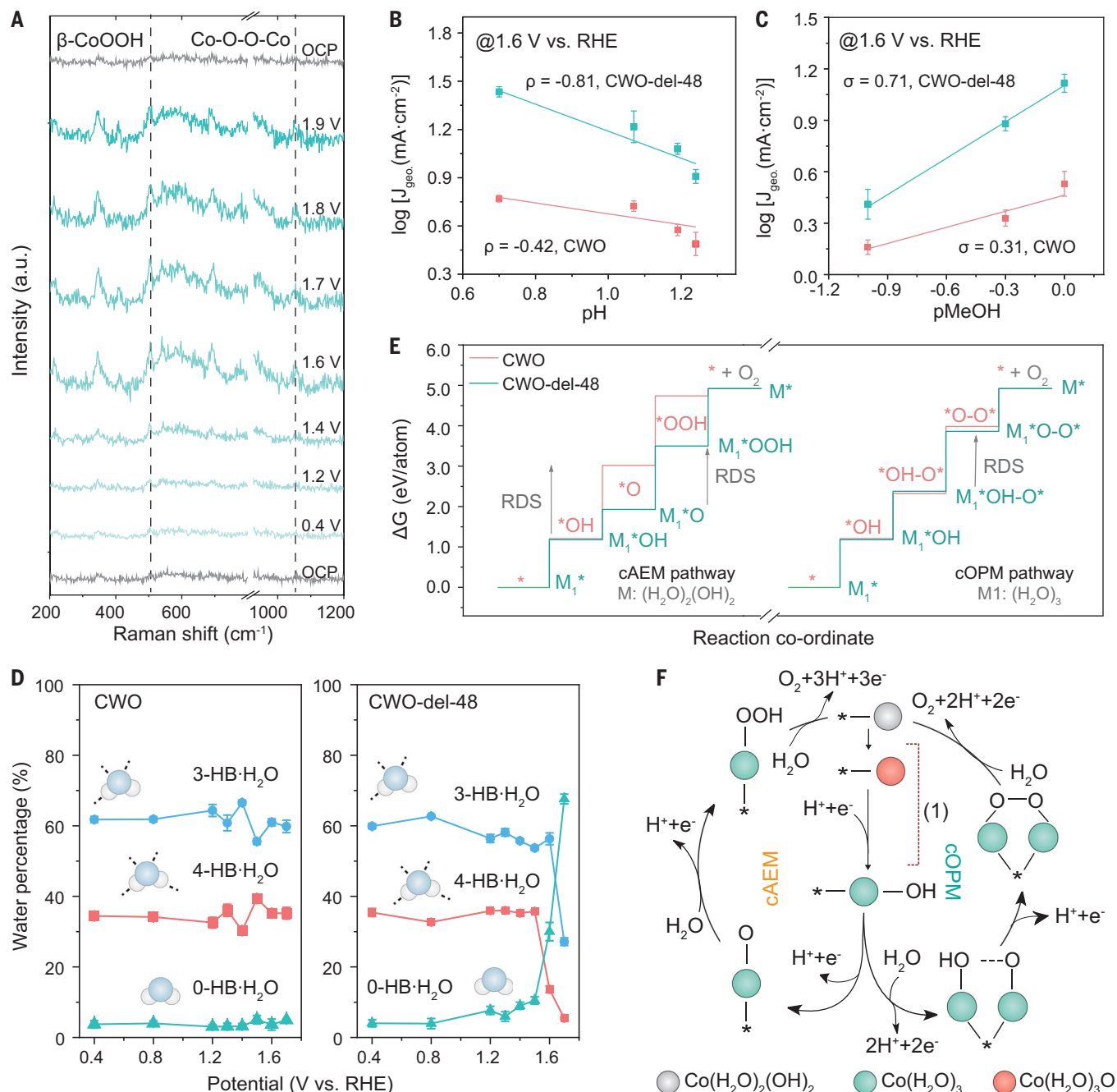
Fig. 3. OER mechanism—operando and DFT studies. (**A**) Operando Raman spectroscopy in CWO-del-48 (on carbon paper, from OCP to 1.9 V versus RHE in 0.5 M H_2SO_4) reveals a correlation between OER activity and the intensity of β–CoOOH and Co–O–O–Co peaks. (**B** and **C**) pH-dependent studies (1.6 V versus RHE as a function of pH) during OER (B) and MOR (C) elucidate the role of surface-trapped water fragments. Error bars correspond to the standard deviation and average of three independent measurements. (**D**) Percentage of different types of interfacial water structures with applied potential for CWO (left) and CWO-del-48 (right). In CWO-del, the percentage of 0−HB·H$_2$O water increases with applied potential while 4−HB·H$_2$O structure decreases. These remain almost unchanged for CWO in the applied potential window. (**E**) Free energy profiles of CWO and CWO-del-48 in OER pathways. The involved species and/or intermediates are shown in the corresponding steps. The dynamic involvement of H_2O and OH$^-$ enables favorable confined AEM (cAEM) and confined OPM (cOPM) reaction pathways in CWO-del-48. (**F**) OER catalytic cycle schematically showing the cAEM and cOPM pathways. The first step is the chemical conversion of Co(H$_2$O)$_2$(OH)$_2$* to Co(H$_2$O)$_3$O*. Both the cAEM and cOPM mechanisms share Co(H$_2$O)$_3$–OH* as a common intermediate.

and W–O (~886 cm^{-1}) peaks with increasing delamination time (Fig. 2A). The intensity ratio of Co–O to W–O peaks increases up to 48 hours and then saturates (Fig. 2A, inset; fig. S34; and table S8). This suggests a kinetic limitation of W leaching from the CWO matrix. Inductively coupled plasma optical emission spectrometry (ICP-OES) measurements confirm increasing W leaching over time but negligible change in Co concentration (fig. S35 and table S9). The optimal Co/W ratio and OH$^-$ and H$_2$O trapping considering initial electrochemical studies is achieved for 48-hour delaminated samples (see details in later sections). Density functional theory (DFT) simulations show that (010) is the most thermodynamically favorable crystal facet for the delamination process, which is exothermic only at high pH (figs. S36 to S38, tables S10 and S11, and movie S1).

Water trapping and hydroxide bridging

To assess the presence of water and hydroxyl groups in the delaminated samples, we carried out a series of characterizations. Thermogravimetric analysis coupled with mass spectroscopy (TGA-MS) revealed an ~16% weight loss for CWO-del-48 over a 166° to 396°C range due to water and/or OH$^-$ ions, which is negligible for CWO and Co$_3$O$_4$ (Fig. 2B and fig. S39). Four distinct peaks in this range suggest the presence of different water coordination environments (42).

To assess these differently coordinated water populations, we initially performed Fourier transform infrared (FTIR) measurements. These reveal HO–H stretching and H–O–H bending vibrational modes with increasing intensity upon delamination, suggesting a higher density of trapped and bridged water and hydroxide groups within the crystals (fig. S40). Further, the narrow single H–OH stretching peak present in the ex situ Raman spectrum of CWO-del-48 indicates the presence of highly H-bonded water (Fig. 2B, inset, and fig. S41) (43).

Additionally, we replaced H$_2$O with D$_2$O during the delamination process and subjected the samples to mild annealing. This resulted in distinct spectral features corresponding to a D–OD stretching mode, confirming the trapping of D$_2$O or H$_2$O in the delaminated materials (fig. S42) (44).

We studied the resulting oxygen modes using x-ray photo electron spectroscopy (XPS) (Fig. 2C). The O 1s peak of nondelaminated samples deconvolutes into two peaks at 528.55 and 530.33 eV, which correspond to metal oxygen (O$_M$) and lattice oxygen (O$_L$) (25). CWO-del-48 spectra, on the other hand, require deconvolution into two additional peaks corresponding to hydroxide (O$_{OH}$, at 531.6 eV) and water species (O$_{H_2O}$, at 533.1 eV) (35). The O$_M$ and O$_L$ peaks blue shift in this case, which is consistent with the leaching of W in the form of

WO$_4{}^{2-}$ and associated atomic vacancies (O$_M$) (45); this is also supported by ultraviolet-visible (UV-Vis), electron paramagnetic resonance (EPR), and x-ray absorption near-edge structure (XANES) spectra (figs. S15 to S19). The amplitude of O$_{OH}$ and O$_{H_2O}$ signals further suggests the presence of hydroxide and bonded water in the delaminated compound.

To gain insights into the role of delamination and water-hydroxide trapping in rendering catalyst stability, we carried out DFT studies considering water trapping and hydroxide bridging from WO$_4{}^{2-}$ sites transformation (movie S1 and fig. S12). Because the size of water-trapped structures can also vary, various combinations of structures with different numbers of water molecules and OH$^-$ were calculated. Among the different combinations of CWO-water-hydroxide, Co(WO$_4$)$_{1-x}$(H$_2$O)$_2$(OH)$_2$ is the thermodynamically most-favorable delaminated species, with a –4.5 eV of Gibbs free energy change for the transformation (Fig. 2D and tables S12 and S14). The calculated Pourbaix diagram (Fig. 2E) confirms the stability of this phase over other structures at pH 0.

The blue shift observed in XANES and distinct extended x-ray absorption fine structure (EXAFS) spectra implies a higher oxidation state of Co and a modified coordination environment in CWO-del-48 compared with CWO (figs. S18 and S19). The corresponding Co–O and Co–Co bond distance of the CWO-del-48 structure are shorter than those in CWO (Fourier-transformed EXAFS, fig. S19; crystal structure, fig. S43), which could facilitate higher-valence Co species, such as CoOOH and Co–peroxide, in OER (20, 31, 46).

In situ Raman spectroscopy in 0.5 M H$_2$SO$_4$ electrolyte reveals three oxide peaks at 1.7 V [versus reversible hydrogen electrode (RHE)] (supplementary text, section 6, and tables S2 and S3), some of which are not visible in ex situ Raman spectra (Fig. 2F). These correspond to layered β–CoOOH (~502 cm^{-1}), γ–CoOOH (~571 cm^{-1}), higher-oxidation Co^{IV}–O (~840 cm^{-1}), and Co–peroxide (~1080 cm^{-1}) sites (46–48), in agreement with EXAFS, XPS, and DFT findings (Fig. 2C and figs. S19 and S44).

Structural influence on the OER mechanism

To gain more insights into the peroxide species and the nature of the active sites ensuing from OH$^-$ and H$_2$O trapping, we performed additional operando Raman spectroscopy studies before and after OER onset potential (Fig. 3A and fig. S43). Both β–CoOOH and Co–peroxide peak intensities steadily increase from open circuit potential (OCP) to 1.9 V versus RHE and vanish as the potential is cycled back to OCP from 1.9 V versus RHE (Fig. 3A). This suggests that both β–CoOOH and Co–peroxide are active sites for the OER. To investigate the role of the surface oxides and water-hydroxide trapping in the OER activity, we carried out a

suite of pH-dependent electrochemical studies and operando interfacial water structure evaluation using Raman spectroscopy.

Delaminated samples display a very strong pH dependence during the OER, with a reaction order (ρ) of –0.84, nearly 2.5 times that for CWO (Fig. 3B). This can be explained by the presence of trapped water and a higher OH$^-$ coverage, in agreement with both XPS (Fig. 2D) and FTIR studies (fig. S40). The calculated cross-sectional crystal structure (fig. S43) and XPS analysis (fig. S45) suggest a CoOOH-rich arrangement, where water is bonded with Co atoms through the oxygen. This is consistent with Raman spectra and methanol oxidation reaction (MOR) experiments, showing a dominance of MOR over water dissociation in CWO-del-48 across different pH values, in line with the higher amount of surface oxides (Fig. 3C) (49).

Next, we studied the role of interfacial H–OH using operando Raman spectroscopy (figs. S46 and S47), deconvoluting three different water structures depending on the number of H bonds: 4-H–bonded water (~3200 cm^{-1}), 3-H–bonded water (~3400 cm^{-1}), and 0-H–bonded water (~3600 cm^{-1}). The activation energy required for water dissociation is predicted to decrease with decreasing degree of H bonding (39). As the potential increases from 0.4 to 1.7 V versus RHE, the relative presence of 4–HB H$_2$O in CWO-del-48 decreases from 35 to 5%, whereas 0–HB H$_2$O increases from 4 to 68% (Fig. 3D). By contrast, these remain unchanged for CWO throughout the applied potential window. This observation suggests the involvement of interfacial water in the rate-determining step (RDS) for the CWO-del-48 catalyst. Moreover, the substantial change in the Stark slope explains the higher sensitivity of interfacial water structure after OER onset potential (fig. S48).

On the basis of these experimental observations, we performed DFT calculations to assess the energy landscape of the OER mechanisms using the computational hydrogen electrode (CHE) formalism (Fig. 3E). We denote the paths where the confined water fragments can also participate as confined paths. The oxide path mechanism (OPM) has a common RDS (*OH–O* to *O–O*) for both CWO and for the confined water fragments in CWO-del-48 without involving interfacial water. The RDS for CWO-del-48 is 0.09 eV smaller for the OPM pathway than for the adsorbate evolution mechanism (AEM), which makes it thermodynamically more plausible. In the AEM pathway (supplementary text, section 4), the RDS is however different: OH*-to-O* for CWO versus the confined system cAEM and O*-to-OOH* for CWO-del-48 (tables S14 to S17). The higher pH dependence and change of the interfacial water structure with increasing applied potential for CWO-del-48, suggests that CWO-del-48 benefits from the kinetically favorable AEM mechanism (Fig. 3F and fig. S17).

To gain insights into the improved acid resistance under electrolytic conditions, we revisited the surface Pourbaix diagram of CWO-del (Fig. 2E). This diagram is divided into five distinct regions: region I, $CWO(H_2O)_2(OH)_2$; region II, $CWO(H_2O)_3OOH^*$; region III, $CWO(H_2O)_3OH^*O^*$; region IV, $CWO(H_2O)_3{}^*OO^*$; and region V, $CWO(H_2O)_3O^*$ (details in fig.

S49). In conditions of low pH, the H^+ ions from the acidic environment interact with H_2O–OH cluster in $CWO(H_2O)_2(OH)_2$ (region I), which transforms into $CWO(H_2O)_3OH^*O^*$ (region III). When the potential lies between 1.20 and 1.37 V versus RHE, interfacial water molecules (region I) interact with another surface oxygen to form a hydroxyl group: $O^* +$

$H_2O \rightarrow OOH^* + H^+ + e^-$, the cation on the surface undergoes oxidation and is stabilized by OOH*. Simultaneously, the oxygen on the surface binds with H* to create a stable structure of $CWO(H_2O)_3{}^*OO^*$ (region IV), and the two O* species combine directly to form O_2, leading to the release of oxygen without the formation of *OOH intermediate. As the potential
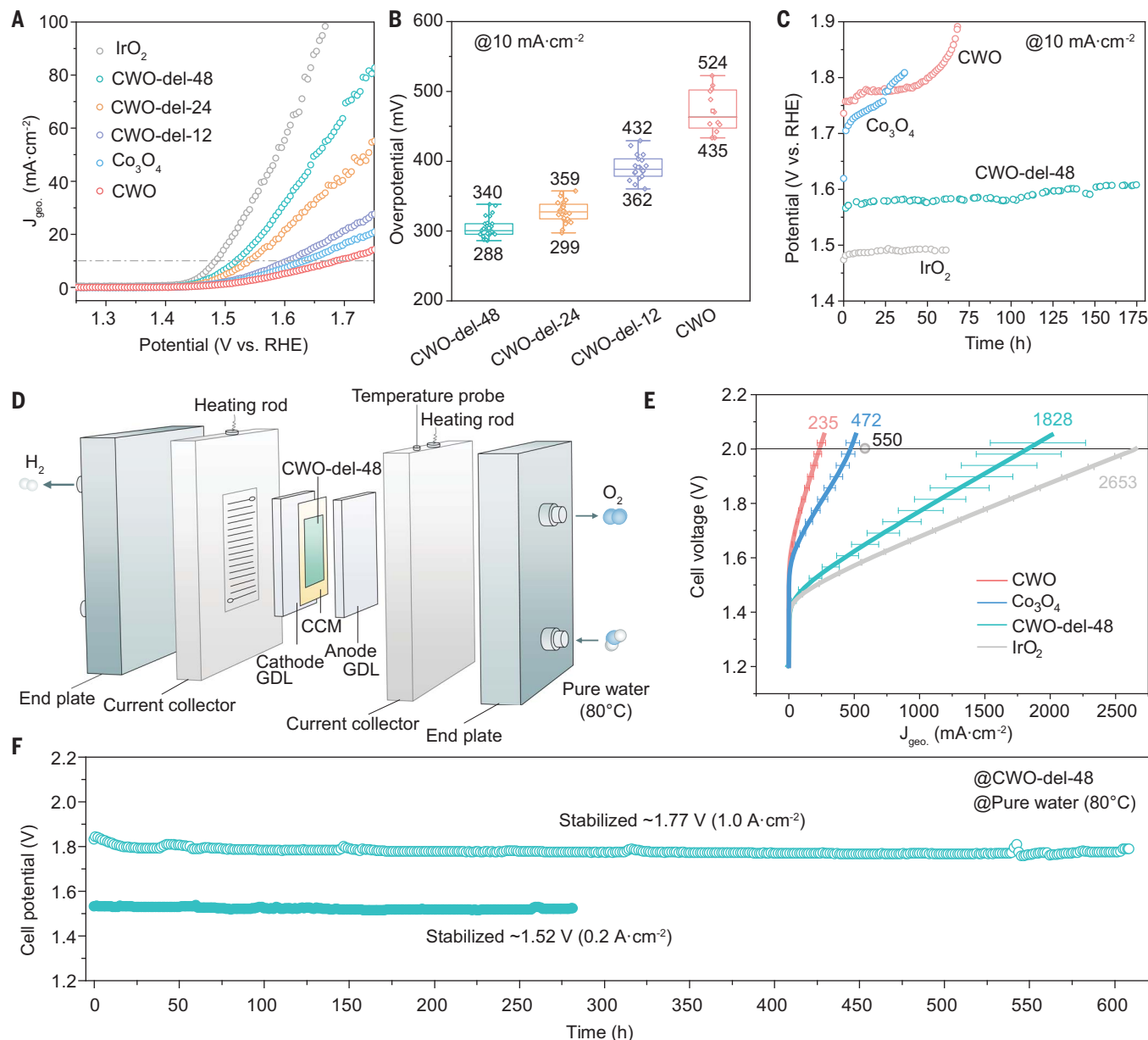
Fig. 4. Electrochemical performance and stable PEMWE at the ampere level. (A) Linear-sweep voltammetry of Co-based catalysts at 5 mV s^{-1} in 0.5 M H_2SO_4 electrolyte along with commercial IrO_2 and Co_3O_4 (no *iR* correction). **(B)** Overpotential statistics at 10–mA cm^{-2} current density. **(C)** Chronopotentiometry stability tests in 0.5 M H_2SO_4 electrolyte at constant 10–mA cm^{-2} current density in H-cell setup using a Nafion 117 membrane. **(D)** Illustration of PEMWE along with catalyst-coated membrane (CCM), cathode, and anode GDL. **(E)** The PEMWE-based polarization curves of CWO-del-48, CWO, commercial Co_3O_4, and IrO_2 (without *iR* correction) used as anodic material

separately. The PEMWE-based polarization curve is compared with the best reported, La-Mn codoped porous cobalt spinel fibers catalyst (*25*). Commercial 60 wt % Pt/C was used as cathodic material, and Nafion 117 is the membrane. **(F)** The chronopotentiometry stability test of CWO-del-48 at 0.2 A cm^{-2} and at 1.0 A cm^{-2} of current density in PEMWE at 80°C temperature for 278 hours and 608 hours, respectively, after overnight conditioning at 1.7 V (see supplementary text for details). The milli-Q water filling process during operation leads to small voltage transients due to temperature gradients and interface re-equilibration.

rises to ≥1.46 V (versus RHE), the surface is shielded by O*, leading to the formation of a stable $CWO(H_2O)_3O*$ structure (region V).

Electrochemical performance

We compared the polarization curves of CWO-del catalysts with commercial Co_3O_4 and IrO_2 (Fig. 4A) (supplementary text, section 6). A minimum 288-mV overpotential at 10–mA cm^{-2} current density was obtained for CWO-del-48 [no iR (i, current; R, resistance) correction], as opposed to 392 and 259 mV for commercial Co_3O_4 and IrO_2, respectively (see figs. S50 to S52 and table S18 for details on particle size, loading, and double-layer capacitance). Statistical analysis (Fig. 4B) and extended measurements confirm the reproducibility of these trends (figs. S53 and S54). The Faradaic efficiency for O_2 generation was 96.6 ± 5.2% at 10–mA cm^{-2} current density (figs. S55 to S60).

Tafel analysis reveals a slope of 85 mV decade^{-1} for CWO-del-48 versus 63 mV decade^{-1} for IrO_2 and 227 mV decade^{-1} for CWO. This showcases the improved OER kinetics of CWO-del-48 over reference samples, approaching that of IrO_2 (fig. S61).

CWO-del-48 exhibits the highest stability (>175 hours) over commercial Co_3O_4 and CWO (Fig. 4C) in a H-cell at 10 mA cm^{-2}. Structural, compositional, and electrochemical postanalysis, suggest that the crystallinity, microstructure, and size remain comparable after electrolysis (figs. S24 and S62 to S67 and table S19).

We then assessed Co leaching and the potential role of dissolved species. Inductively coupled plasma mass spectroscopy (ICP-MS) reveals that Co leaching remains unchanged after 50 hours of OER in a H-cell at 10 mA cm^{-2} with an ~2.76 parts per million (ppm) concentration of dissolved Co ions in anolyte after 100 hours of chronopotentiometry (fig. S68). A fraction of Co ions (0.3 ppm) leaches out during OCP, before the OER stability test. The concentration of dissolved Co ions in the catholyte remained negligible [<30 parts per billion (ppb); fig. S69], and no traces were found in the membrane (fig. S70 and table S20) or graphite rod (fig. S71). The resulting stability number (S number) (50, 51) after 100 hours of stability test at 10 mA cm^{-2} is 14771 ± 768 (fig. S72). Additional experiments confirm the electrochemical stability at different mass loadings (0.075 to 2 mg cm^{-2}) (figs. S73 and S74).

Encouraged by this, we implemented the CWO-del-48 catalyst in a PEMWE system (Fig. 4D and fig. S75) and studied the cell performance under industrial operational settings, including 80°C temperature and a high current density of 0.2 to 1 A cm^{-2} (see supplementary text, section 6, for details). The polarization curve of CWO-del-48–based cells reaches a nominal current density of 1.8 A cm^{-2} at 2 V (Fig. 4E)—an improvement in rate over the previous-best Ir- and Ru-free anodes of up to 3× for a com-parable membrane (25) and of 1.8× for advanced, thinner membranes (40).

During electrolysis at a fixed current density of 0.2 A cm^{-2}, the voltage range (1.53 to 1.56 V) is ~130 mV lower than prior-best Co-based PEMWE catalysis (Fig. 4F) and matches that of Ir black (1.50 V) at one-quarter the loading. This showcases the potential of CWO-del-48 catalysts compared with the well-established iridium oxide, along with its lower cost and potentially higher availability of Co and W. This performance (~1.52 V at 0.2 A cm^{-2}) is retained for at least >278 hours of continuous operation (limited by pump failure).

ICP-OES analysis of the anolyte reveals a Co concentration of ~1.7 ppm after 20 hours of electrolysis (fig. S76). We also performed single-pass electrolyte flow experiments to study the potential role of ion accumulation in the electrolyte reservoir. The cell voltage remains stable (within 1.53 to 1.54 V) for at least 32 hours at 0.2 A cm^{-2} at similar PEMWE conditions but with continuous, fresh electrolyte flushing (fig. S77).

We further challenged the stability of the CWO-del-48 catalyst at 1–A cm^{-2} operation (Fig. 4F)—a so far elusive benchmark for Ir- and Ru-free catalysts. Electrodes show comparable composition after an initial 20 hours of study (figs. S78 to S81 and table S21). The PEMWE cell exhibited stable performance with a stabilized cell voltage of ~1.77 V during 608 hours of durability study (see table S22 for prior benchmarks). The observed slight voltage fluctuations might arise as a result of a combination of temperature gradients during electrolyte replenishment, modifying electrolysis rates and gas dissolution, and catalyst dissolution (ion and particulate detachment) events.

The calculated S number at these conditions is ~31% of that achieved at 10 mA cm^{-2} in the H-cell (supplementary text). This showcases the impact of high rate and temperature operation stress, which accelerate catalyst degradation.

Conclusion and future scope

The reported strategy still faces several challenges and opportunities. CWO-del samples exhibit high polarization voltage under high current density, which should be improved by further optimization of the integration of key components to enhance electrolysis performance and subsequently improve stability at higher currents that approach state-of-the-art Ir systems.

In the future, achieving industrial performance benchmarks, such as energy-efficient and stable operation in the 2– to 3–A cm^{-2} range (a milestone of IrO_2 in PEMWE) will require tailored engineering of catalysts electrodes and membranes. In that sense, obtaining further insights into the properties of these interfaces and into the roles of water trapping and hydroxide bridging in the OER at increasing current densities will be crucial. Operando spectroscopies and modeling at these settings are fundamental enabling tools that can help in that direction. Quantifying the catalyst dissolution dynamics through inline ICP-MS studies, under relevant PEMWE target conditions, is crucial to further understand the local dissolution-redeposition equilibria. Combined with morphology and elemental analysis, this could help elucidate the dissolution pathways through accelerated stress tests (52).

Progressing toward fully Earth-abundant metal PEMWE catalysts—including the cathodic side—and recyclable systems demands further innovation, spanning materials, electrode structures, membrane-electrode interfaces, and process control. Whereas this study focuses on abundant Co-based OER catalysts, further advances in alternative materials (e.g., Mn and Ni), which consider geopolitical barriers and environmental aspects related to metal extraction and purification, remain urgently needed.

REFERENCES AND NOTES

1. S. Chu, A. Majumdar, *Nature* **488**, 294–303 (2012).
2. I. Staffell et al., *Energy Environ. Sci.* **12**, 463–491 (2019).
3. Z. W. Seh et al., *Science* **355**, eaad4998 (2017).
4. M. Carmo, D. L. Fritz, J. Mergel, D. Stolten, *Int. J. Hydrogen Energy* **38**, 4901–4934 (2013).
5. C. Spöri, J. T. H. Kwan, A. Bonakdarpour, D. P. Wilkinson, P. Strasser, *Angew. Chem. Int. Ed.* **56**, 5994–6021 (2017).
6. L. An et al., *Adv. Mater.* **33**, e2006328 (2021).
7. P. C. K. Vesborg, T. F. Jaramillo, *RSC Adv.* **2**, 7933–7947 (2012).
8. L. Yang et al., *Nat. Commun.* **9**, 5236 (2018).
9. Y. Pi, Q. Shao, P. Wang, J. Guo, X. Huang, *Adv. Funct. Mater.* **27**, 1700886 (2017).
10. S. Cherevko et al., *ChemCatChem* **6**, 2219–2223 (2014).
11. E. A. Paoli et al., *Chem. Sci.* **6**, 190–196 (2015).
12. A. Grimaud et al., *Nat. Chem.* **9**, 457–465 (2017).
13. Z.-Y. Wu et al., *Nat. Mater.* **22**, 100–108 (2023).
14. L. C. Seitz et al., *Science* **353**, 1011–1014 (2016).
15. S. Hao et al., *Nat. Nanotechnol.* **16**, 1371–1377 (2021).
16. Y. Wang et al., *ACS Appl. Mater. Interfaces* **12**, 37006–37012 (2020).
17. H. Liu et al., *Joule* **7**, 558–573 (2023).
18. M. W. Kanan, D. G. Nocera, *Science* **321**, 1072–1075 (2008).
19. J. B. Gerken et al., *J. Am. Chem. Soc.* **133**, 14431–14442 (2011).
20. Z.-F. Huang et al., *Nat. Energy* **4**, 329–338 (2019).
21. B. Zhang et al., *Nat. Catal.* **3**, 985–992 (2020).
22. B. Zhang et al., *Science* **352**, 333–337 (2016).
23. S. Pan et al., *Nat. Commun.* **13**, 2294 (2022).
24. J. Huang et al., *Nat. Commun.* **12**, 3036 (2021).
25. L. Chong et al., *Science* **380**, 609–616 (2023).
26. A. Li et al., *Angew. Chem. Int. Ed.* **58**, 5054–5058 (2019).
27. I. A. Moreno-Hernandez et al., *Energy Environ. Sci.* **10**, 2103–2108 (2017).
28. I. C. Man et al., *ChemCatChem* **3**, 1159–1165 (2011).
29. J. S. Mondschein et al., *Chem. Mater.* **29**, 950–957 (2017).
30. M. Etzi Coller Pascuzzi, M. van Velzen, J. P. Hofmann, E. J. M. Hensen, *ChemCatChem* **13**, 459–467 (2021).
31. N. Wang et al., *J. Am. Chem. Soc.* **145**, 7829–7836 (2023).
32. M. Chatti et al., *Nat. Catal.* **2**, 457–465 (2019).
33. P.-Y. Cheng et al., *J. Colloid Interface Sci.* **623**, 327–336 (2022).
34. B. Rodríguez-García et al., *Sustain. Energy Fuels* **2**, 589–597 (2018).
35. Y. Wen et al., *Nat. Commun.* **13**, 4871 (2022).
36. J. Rossmeisl, Z.-W. Qu, H. Zhu, G.-J. Kroes, J. K. Nørskov, *J. Electroanal. Chem.* **607**, 83–89 (2007).
37. Y. Ping, R. J. Nielsen, W. A. I. I. I. Goddard III, *J. Am. Chem. Soc.* **139**, 149–155 (2017).

38. L. F. Shen et al., . Angew. Chem. Int. Ed. **59**, 22397–22402 (2020).
39. Y.-H. Wang et al., Nature **600**, 81–85 (2021).
40. S. Kong et al., Nat. Catal. **7**, 252–261 (2024).
41. L. Gao et al., Chem. Mater. **32**, 1703–1747 (2020).
42. S. E. Kelch et al., J. Phys. Chem. C **125**, 26552–26565 (2021).
43. K. Oka et al., Sci. Rep. **9**, 223 (2019).
44. Q. Hu, H. Zhao, S. Ouyang, Phys. Chem. Chem. Phys. **19**, 21540–21547 (2017).
45. C.-Q. Li et al., J. Mater. Chem. A **7**, 17974–17980 (2019).
46. A. Moysiadou, S. Lee, C.-S. Hsu, H. M. Chen, X. Hu, J. Am. Chem. Soc. **142**, 11901–11914 (2020).
47. C. Jing et al., ACS Catal. **12**, 10276–10284 (2022).
48. M. Zhang, M. de Respinis, H. Frei, Nat. Chem. **6**, 362–367 (2014).
49. H. Liu et al., Sci. Rep. **7**, 11421 (2017).
50. S. Geiger et al., Nat. Catal. **1**, 508–515 (2018).
51. C. Wei et al., ACS Catal. **13**, 14058–14069 (2023).
52. M. Milosevic et al., ACS Energy Lett. **8**, 2682–2688 (2023).
53. H. Benzidi, Co-del_OER, ioChem-BD (2024); https://doi.org/10.19061/iochem-bd-1-320.
54. R. Ram, F. P. García de Arquer, STEM and XRD files of Water and Hydroxide Trapping in Cobalt Tungstate for Proton Exchange Membrane Water Electrolysis, Data set, Zenodo (2024); https://doi.org/10.5281/zenodo.11161891.

SUPPLEMENTARY MATERIALS

science.org/doi/10.1126/science.adk9849
Supplementary Text
Figs. S1 to S81
Tables S1 to S22
References (55–67)
Movie S1